

# physica **p** status **s** solidi **s**

[www.pss-journals.com](http://www.pss-journals.com)

**reprint**



# Silicon nanocrystals for nonlinear optics and secure communications

## Feature Article

Z. Bisadi<sup>1</sup>, M. Mancinelli<sup>1</sup>, S. Manna<sup>1</sup>, S. Tondini<sup>1</sup>, M. Bernard<sup>1,2</sup>, A. Samusenko<sup>1,2</sup>, M. Ghulinyan<sup>2</sup>, G. Fontana<sup>1</sup>, P. Bettotti<sup>1</sup>, F. Ramiro-Manzano<sup>1</sup>, G. Pucker<sup>2</sup>, and L. Pavesi<sup>\*1</sup>

<sup>1</sup> Department of Physics, Nanoscience Laboratory, University of Trento, Trento, Italy

<sup>2</sup> Centre of Materials and Microsystems, Bruno Kessler Foundation, Trento, Italy

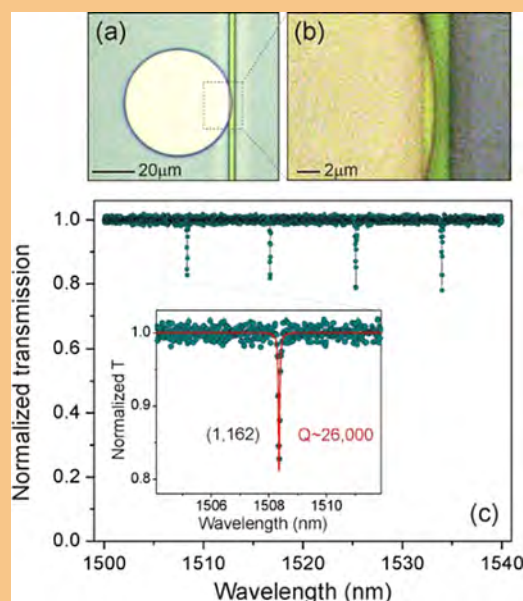
Received 24 July 2015, revised 22 September 2015, accepted 25 September 2015

Published online 14 October 2015

**Keywords** nanocrystals, nonlinear optics, photonics, secure communication, silicon

\* Corresponding author: e-mail lorenzo.pavesi@unitn.it, Phone: +390 461 281605, Fax: +390 461 282921

Silicon nanocrystals (Si-nc) are reviewed here for their interesting optical applications. On the one hand, they do exhibit quantum confinement effects. This allows turning silicon into a light-emitting material where luminescence can be excited by electrical injection. On the other hand, small sizes, large surfaces, and dielectric mismatch between the core and the surrounding matrix increase dramatically the nonlinear optical coefficients. This allows using Si-nc as a nonlinear material in different waveguide configurations. In this paper, we discuss specifically two different applications of Si-nc: (i) as a nonlinear material in various devices, e.g., in bistable optical cavities, in waveguide optical mode monitors that are based on two-photon excited luminescence detection, and in wavelength shifters by using four-wave mixing (FWM); (ii) as an entropy source for quantum random number generation, the key device for cryptography.



(a) Top view optical image of a Si-nc-based whispering-gallery mode (WGM) microdisk resonator, vertically coupled with a bus waveguide. (b) Detail of the coupling zone. (c) Normalized waveguide transmission spectrum over a wide spectral range. The inset shows a blow up of a resonance with the radial and azimuthal mode orders and the  $Q$  factor value indicated.

© 2015 WILEY-VCH Verlag GmbH & Co. KGaA, Weinheim

**1 Introduction** Silicon photonics is thought to be the solution to the interconnect bottleneck and, therefore, has seen an impressive development in recent years [1]. Several examples of the success of the technology are available in the literature: active optical cables have been demonstrated that are able to send data at a speed of

Tbps over a few 100 m span [2]; large-scale integration of electronic–photonic components in a single integrated chip with an integration level in the range of thousands of different components have been fabricated [3]; nanophotonic-based optical networks have been integrated on single chips [4].

In recent years, there has been interest in broadening the opportunities of silicon photonics by looking at new materials or new phenomena. One of the materials that has been extensively investigated is low-dimensional silicon in the form of small silicon nanocrystals (Si-nc) [5]. The reason for this is that Si-nc show quantum size effects and can be produced by CMOS compatible processes. In this feature paper, we will review Si-nc, detailing their use as a nonlinear material or as an entropy source in quantum random number generators.

**1.1 Silicon nanocrystals** Si-nc are formed by two main methods: (1) deposition of substoichiometric silicon-rich silicon oxide (SRO) followed by a thermal annealing and (2) chemical synthesis. In the first case, different deposition techniques have been used, the most popular one being plasma-enhanced chemical vapor deposition (PECVD). The chemical route follows a disproportionation of  $\text{SiO}_{1.5}$ -type precursors. The most commonly used precursors are hydrogen silsesquioxane (HSQ) or sol-gel polymer derived from hydrolysis of  $\text{HSiCl}_3$  [6–8].

**1.2 Si-nc properties** The small size, in the few nanometer range, of Si-nc causes different properties with respect to crystalline bulk Si. The most evident one is the bright red emission at room temperature that is absent in bulk silicon. In the following, we list the main properties of Si-nc:

(i) Light emission [5]: the increased emission efficiency of silicon nanocrystals with respect to bulk

silicon is due to three factors. First, the quantum confinement of electrons and holes in quantum dots causes an increased overlap of their wavefunctions in the k-space. This, in turn, implies large radiative recombination probabilities. In fact, the typical luminescence decay for Si-nc is in the microsecond time range, in comparison with the radiative lifetime of bulk silicon that is in the 10 ms range. In addition, the quantum confinement causes a red shift of the emission that is also size dependent. Secondly, the decreased effective refractive index of the  $\text{SiO}_2/\text{Si-nc}$  composite increases the escape probability of photons from the material. Thirdly, the spatial confinement of carriers in small space regions decreases their diffusion. This results in a decreased probability for the excited carriers to encounter nonradiative recombination centers. Therefore, Si-nc are characterized by large internal quantum efficiency. Internal quantum efficiencies of up to 100% have been reported for ligand-passivated silicon nanocrystals [44].

(ii) Optical gain [9]: interface states due to the formation of Si–O double bonds at the surface of the Si-nc allow for the formation of a four-level system that can be inverted to yield positive optical gain. The delicate balance between stimulated emission and nonradiative recombination hinders a clearcut strategy to optimize the gain. In addition, as will be discussed later, electrical injection is difficult in the system. Therefore, various reports on optically pumped gains have been published, although none on electrically injected lasers.

(iii) Nonlinear optical effects [10]: the dielectric mismatch between the crystalline-silicon core and the amorphous embedding silica matrix causes a local field enhancement of the optical waves. This, in turn, yields an enhancement of the nonlinear optical properties of Si-nc in  $\text{SiO}_2$ . Furthermore, nonlinearity in Si-nc is also increased by quantum size effects. Therefore, many reports on the Si-nc optical nonlinearities due to second- and third-order susceptibility have appeared (see Section 3).

(iv) Photoresponse [11]: light is absorbed in Si-nc by free carriers that diffuse in the matrix by hopping, direct tunneling, or Fowler–Nordheim tunneling. In this way, both photoconductivity as well as photovoltaic effects manifest in Si-nc-based materials. Indeed, Si-nc have been used in solar cells either to realize tandem cells or as a downshifting layer. The downshifting layer is used as a sun spectrum reshaper in order to move optical radiation from the blue region, where silicon solar cells have a low-conversion efficiency, to the red, where silicon solar cells have an almost unitary conversion efficiency. Tandem cells based on Si-nc have a disappointing low efficiency mostly caused by the poor conductivity of the system. On the other hand, a very strong increase of the efficiency of silicon cells has been reported when an engineered Si-nc layer has been used as a downshifting layer [12].

(v) Biocompatibility [13]: silicon is biocompatible. Si-nc are biocompatible and are used in animals because they are biodegradable. When the surface of Si-nc is



**Lorenzo Pavesi** is Professor of Experimental Physics and head of the Department of Physics at the University of Trento, Italy. Born in 1961, he received his PhD in physics in 1990 at the Ecole Polytechnique Federale de Lausanne, Switzerland. In 1990, he became Assistant Professor, an Associate Professor in 1999, and Full Professor in 2002 at the University of Trento. He leads the Nanoscience Laboratory. He founded the research activity in semiconductor optoelectronics at the University of Trento and started several laboratories of photonics, growth, and advanced treatment of materials. During the last few years, he concentrated on silicon-based photonics where he looks for the convergence between photonics and electronics. He is interested in active photonics devices which can be integrated in silicon by using optical nonlinearities and modified material properties. His interests also encompass optical sensors or biosensors and solar cells. The recent development is toward integrated quantum photonics. He holds an H-number of 51 according to the web of science and of 60 according to Google Scholar.

functionalized, Si-nc preserve their emission properties and can be used as biomarkers or as chromophores in bioimaging experiments. More interestingly, drugs can be drafted on the Si-nc surface and released in specific compartments that makes them a traceable drug-delivery system [14].

(vi) Sensitization action: Si-nc can be used as a sensitizer of other active emission centers [15]. A typical example is the coupled system of Er ions and Si-nc. Er, a rare-earth element, in its trivalent state ( $\text{Er}^{3+}$ ) shows a photoluminescence band at  $1.55\ \mu\text{m}$ , due to the  $^4\text{I}_{13/2} \rightarrow ^4\text{I}_{15/2}$  transition. This transition is metastable and, therefore, can be used to make a four- or a three-level laser system. However, the excitation cross section of Er is extremely small. This can be increased by many orders of magnitude when Si-nc are coupled with Er in such a way that both optical excitation and electrical excitation produce strong emission. The same sensitization role is played by Si-nc with respect to other color centers, and active research is underway to investigate phosphors made by Si-nc and other impurities.

**2 Silicon nanocrystals embedded in a microresonator** Si-nc-based microdisk structures have been scarcely studied and only a few studies have appeared in the literature [16, 17]. In a microdisk resonator, light is trapped due to total internal reflection and propagates within circular trajectories that are named whispering-gallery modes (WGM). These are resonant modes that satisfy the resonant condition  $m\lambda = 2\pi n_{\text{eff}}r$ , where  $m$  is the modal order,  $\lambda$  the resonant wavelength,  $n_{\text{eff}}$  the effective index of the WGM mode, and  $r$  the radius of the disk.

**2.1 Device fabrication** Si-nc-based microdisk resonators can be produced using standard silicon micro-fabrication technology [18, 19]. As an example, a 135 nm thick SRO layer is first deposited on top of a crystalline silicon wafer from a mixture of silane ( $\text{SiH}_4$ , 65 sccm) and nitrogen oxide ( $\text{N}_2\text{O}$ , 973 sccm) gases using a parallel-plate PECVD chamber. A successive 1 h annealing in an  $\text{N}_2$  atmosphere at  $1100\ ^\circ\text{C}$  leads to the formation of Si-nc within the  $\text{SiO}_x$  host (with  $\sim 10\%$  of Si atoms in the nanocrystalline phase) [9]. Then, the wafers are photolithographically patterned and dry etched anisotropically using  $\text{CHF}_3/\text{SF}_6$  gas chemistry. As a result, arrays of microdisk structures with diameters ranging from 2 to  $10\ \mu\text{m}$  are formed. Isolation of the microdisks from the silicon substrate is realized via an isotropic wet etch of the substrate to form mushroom-like devices (Fig. 1).

**2.2 Micro-PL from single-WGM resonators** Room-temperature micro-PL measurements were performed using the 488 nm line of an argon laser tightly focused on the microdisk array in order to optically pump single devices. The emitted signal was collected in the plane of the disk, selected with a polarizer, and sent to a CCD.

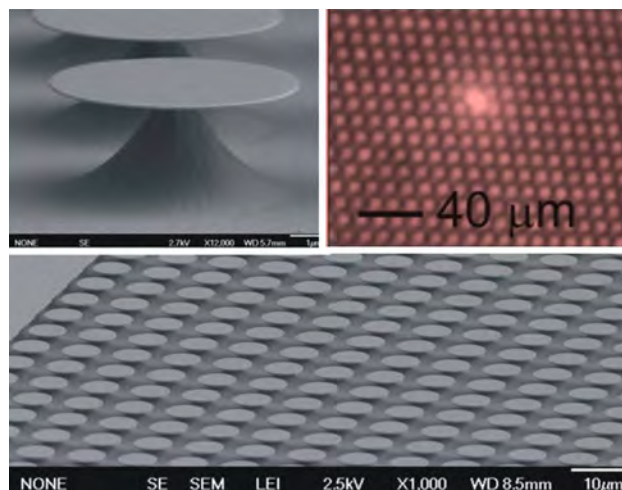


**Figure 1** SEM images of the microdisk array and of a single device. (Top right) The out-of-plane emission from a single device that is optically excited.

The in-plane emission spectrum from a microdisk shows a typical broadband emission due to the background PL, which is uncoupled with the WGM modes, on which fine features, originating from the resonator modes, are superimposed (Fig. 2). These modes manifest as emission lines with subnanometer full width at half-maximum (FWHM), leading to quality factors  $Q \cong 3 \times 10^3$ . These  $Q$  values are limited by the spectral resolution of the micro-PL setup. A higher precision measurements reveals  $Q$  of up to 7000 (Fig. 2, inset). The spectral interval, where high  $Q$  factors are observed, is limited by the trade-off between a lower material absorption and a weaker confinement of resonator modes at long wavelengths, and by the decrease of

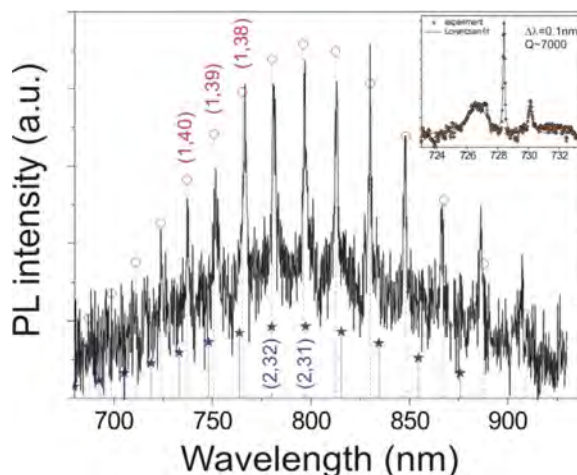


**Figure 2** Measured TE-polarized WGM spectrum of an  $8\ \mu\text{m}$  diameter microdisk plotted together with the simulated peak positions for the first radial mode family (empty circles). The predicted second mode family (full stars) is weak and barely visible in the measured spectrum. (Inset) A high-resolution spectrum of the first family mode with a  $Q \sim 7000$ .

the emission of the nanocrystals at short wavelengths. In particular, at long wavelength the WGM spills out from the resonator, which increases the radiation losses and, in turn, decreases the cavity  $Q$  factors.

**2.3 Pump-power dependence of mode  $Q$  factors** A strong influence of the pumping power on the modal characteristics of Si-nc-based microdisk resonators was manifested in terms of significant line-width modification. A monotonic, roughly 13-fold, reduction of  $Q$  factors was recorded as the pump power increases from 1.25 to 100 mW (Fig. 3a).

The  $Q$  factor reduction suggests that either additional losses are introduced or enhancement of the existing ones takes place at high excitation powers. In a resonator, the total losses, resulting from different loss mechanisms, can

be expressed through the sum of the inverse of the possible limiting  $Q$  factors

$$Q_{\text{tot}}^{-1} = Q_{\text{mat}}^{-1} + Q_{\text{rad}}^{-1} + Q_{\text{ssc}}^{-1} + Q_{\text{sa}}^{-1}, \quad (1)$$

where the inverse of  $Q_{\text{mat}}$ ,  $Q_{\text{rad}}$ ,  $Q_{\text{ssc}}$ , and  $Q_{\text{sa}}$  stand for material (bulk absorption and propagation), radiation, surface scattering, and surface absorption losses, respectively. The last three loss contributions are considered to be independent of the pump power within a good approximation, while  $1/Q_{\text{mat}}$  does not.

Therefore, the increase of the losses is due to the power-dependent  $Q_{\text{mat}}$ . The material  $Q$  factor is defined as  $Q_{\text{mat}} = 2\pi n_g / (\lambda \alpha)$ , with  $n_g$  being the group index and  $\alpha$  the material loss coefficient. In recent studies on Si-nc containing waveguides, pump-power-induced losses at 1.5  $\mu\text{m}$  wavelength have been measured and attributed to excited carrier absorption (ECA) [20]. We believe that the same mechanism also occurs at the Si-nc emission wavelengths. Si-nc absorb strongly at visible wavelengths creating an exciton. Part of the excitons can successively absorb other photons to promote electrons to higher energetic levels in the nanocrystal conduction band. Such absorption will enhance the cavity losses, causing the observed mode broadening. Under low-pump conditions, the ECA loss is expected to increase linearly with power,  $P$ . At high-pump powers, different phenomena can deviate from this simple relationship. A number of processes, such as the ECA itself (reabsorption of either a pump or emitted photon by an already formed exciton), Auger recombination and the saturation of the number of excitable nanocrystals, induces additional nonlinear behavior. This nonlinearity has been observed clearly in our experiments. By assuming a power-dependent loss,  $\alpha = \alpha_0 + \alpha^*(P)$ , Eq. (1) can be rewritten as

$$Q_{\text{tot}}^{-1}(P) = \left[ \sum Q_i^{-1} + \frac{\lambda \alpha_0}{2\pi n_{\text{eff}}} \right] + \frac{\lambda \alpha^*(P)}{2\pi n_{\text{eff}}}. \quad (2)$$

In Eq. (2),  $\alpha_0$  stands for the material passive loss coefficient, which has been independently estimated from ellipsometric data and is of the order of 30  $\text{cm}^{-1}$  or less at  $\lambda = 754 \text{ nm}$  (note, the quality of the fit to ellipsometric data saturates down to values  $\chi^2 \sim 0.1$  for loss coefficients smaller than  $\alpha_0 = 30 \text{ cm}^{-1}$ ). The first two terms on the right side of Eq. (2) represent the inverse of  $Q$  of the passive resonator and, as mentioned above, can be considered as a constant term. With this, for the measured data  $Q_{\text{tot}}^{-1}(P)$  a nonlinear fitting function in the form  $\alpha^*(P) = xP/(1 + yP)$ , based on the rate equation model [21], has been applied (Fig. 3b).

The quality of the fit is further confirmed through the following procedure. We consider the fitting value for the passive  $Q$  (the constant term in Eq. (2)), the FDTD-simulated geometrical quality factor  $Q_{\text{rad}} \approx 1.1 \times 10^4$  for 8  $\mu\text{m}$  disks and negligible surface scattering/surface absorption losses, and backcalculate the material passive

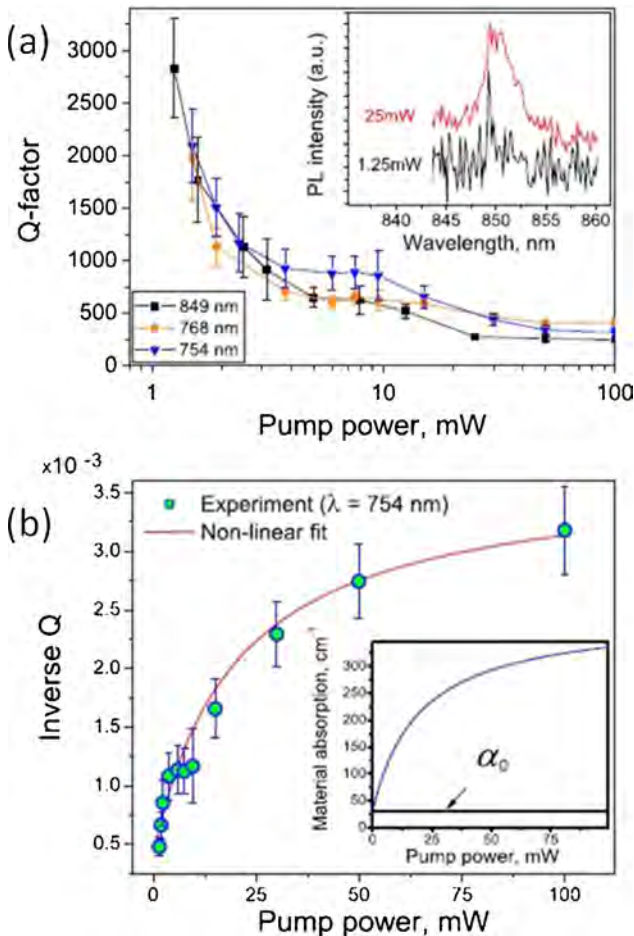


**Figure 3** Pump-induced excited carrier absorption in Si-nc and modification of mode  $Q$  factors: (a) the measured  $Q$  versus the pump power are plotted at three different wavelengths, reporting an order of magnitude variation between two extreme pump powers. The inset shows the resonator mode at  $\lambda = 849 \text{ nm}$  at the lowest and at a high pump powers. (b) Nonlinear fit of the measured inverse  $Q_{\text{tot}}^{-1}(P)$  at  $\lambda = 754 \text{ nm}$  using Eq. (2). The inset shows the corresponding power-dependent absorption coefficient  $\alpha = \alpha_0 + \alpha^*(P)$ .

loss coefficient. The thus-obtained  $\alpha_0 \approx 32 \text{ cm}^{-1}$  is in very good agreement with the ellipsometric results.

Thus, we conclude that the ECA figures as the main limiting factor for a possible multiwavelength lasing from the Si-nc-based microdisk resonator. The SRO material optimization (low-loss, positive material gain) should play a key role for further enhancement of the observed  $Q$  factors.

**2.4 Purcell enhancement of Si-nc emission** In this subsection, we report on the direct measurement of the spontaneous emission rate enhancement of Si-nc in microdisk resonators at room temperature [22]. Generally, unlike III–V quantum dots, Si-nc are considered neither as a possible cavity quantum electrodynamic system nor as ideal emitters for emission-rate enhancement observations (Purcell effect) [23]. On the contrary, we have demonstrated experimentally important lifetime reductions (up to 34%) for nanocrystalline emitters coupled to resonances of microdisk resonators with respect to uncoupled ones.

The Purcell enhancement factor  $F_P$  is a typical cavity figure of merit. For an ideal emitter, for which the emitter's intrinsic linewidth  $\Delta\omega_{\text{em}}$  is much smaller than that of the cavity  $\Delta\omega_{\text{cav}}$ , the Purcell enhancement is given as

$$F_P = \frac{3}{4\pi^2} \frac{Q}{V_m} \left(\frac{\lambda}{n}\right)^3, \quad (3)$$

where  $Q$  is the cavity quality factor and  $V_m$  is the mode volume [24]. On the contrary, in a bad emitter regime, i.e.,  $\Delta\omega_{\text{em}} \geq \Delta\omega_{\text{cav}}$ , several considerations and correction factors to Eq. (3) should be taken into account (for details see Ref. [15]). In particular, in such a situation the  $Q$  factor of the cavity has to be replaced by an effective one  $\tilde{Q}^{-1} = Q_{\text{cav}}^{-1} + \frac{\omega_{\text{em}}}{\Delta\omega_{\text{em}}}$ . This generalization considers the influence of the emitter linewidth when it is comparable to that of the cavity.

Usually, time-resolved decay experiments are used to estimate the emission transition rates. For ideal emitters, e.g., III–V quantum dots, the emission decay is described by single-exponential functions, while stretched exponential functions have to be applied in the bad-emitter regimes.

We have measured the PL lifetime of Si-ncs embedded in microdisk resonators by pumping the resonators with a 488 nm line of a kHz-modulated CW laser source. In order to estimate the Purcell enhancement of Si-nc emitters coupled with the cavity modes, we have both monitored the decay of photons at wavelengths resonant with the microdisk resonances as well as at out-of-resonance wavelengths (Fig. 4). In particular, an appreciable difference between peak and dip lifetimes has been measured, resulting in a maximum lifetime shortening of about 34%.

In addition, by comparing our experimental results with the theoretical prediction of Purcell enhancement in a “bad-emitter regime,” effective linewidths of  $\Delta\omega_{\text{em}} \sim 10 \text{ meV}$

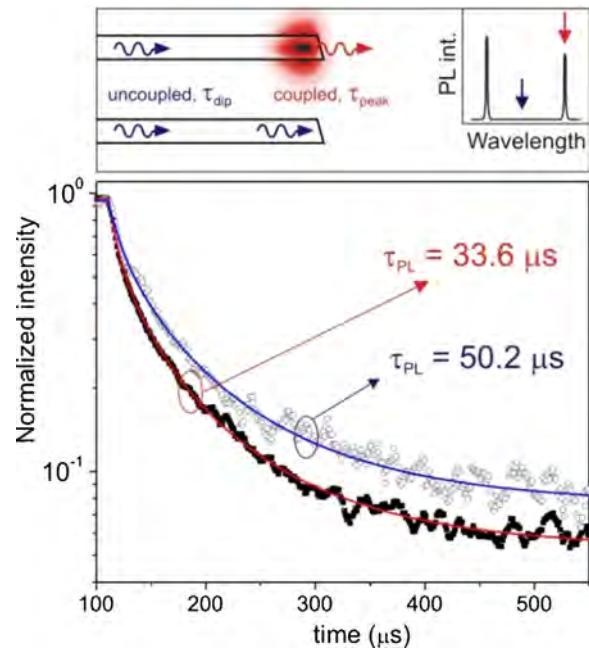


**Figure 4** (Top) Explanation of cavity coupled and uncoupled photons and their relation to the spectral position. (Bottom) The measured out-of-resonance (empty circles,  $\lambda = 846 \text{ nm}$ ) and on-resonance PL signals (full squares,  $\lambda = 853 \text{ nm}$ ). The data have been fitted using single and double stretched exponentials, respectively.

were estimated [22]. Such an emitter linewidth corresponds to  $Q \sim 200$ . This imposes an upper limit to the cavity linewidth that may be efficiently exploited in order to couple Si-ncs to resonator modes. However, the Purcell enhancement can be favored by realizing an ultrasmall mode volume of the cavity and a 25-fold Purcell enhancement can be expected in this case.

### 3 Silicon nanocrystals nonlinear optical properties

Bulk Si-nc show one (two) order of magnitude higher  $\chi^{(3)}$  than silicon (silica) with a moderate absorption. Specifically, at 1550 nm the nonlinear refractive index  $n_2$  of Si is  $n_2 = 4 \times 10^{-14} \text{ cm}^2 \text{ W}^{-1}$ , that of silica is  $n_2 = 2 \times 10^{-16} \text{ cm}^2 \text{ W}^{-1}$  and that of Si-nc is  $n_2 = 4 \times 10^{-13} \text{ cm}^2 \text{ W}^{-1}$  [10]. However, only a few experiments have been performed in this direction.

#### 3.1 Two-photon absorption

Under the condition  $\hbar\omega < E_g$ , one-photon absorption is not possible and two-photon absorption (TPA) comes into play. Therefore, the propagation losses of a waveguide become  $\alpha = \alpha_0 + \beta I$ , where  $\beta$  is the nonlinear loss related to TPA and  $I$  is the laser beam intensity. In a recent study [25], we have measured the nonlinear transmission in single-mode Si-nc waveguides using a TE-polarized 1550 nm pulsed laser. The transmitted power  $P_{\text{out}}$  varies as a function of the input power  $P_{\text{in}}$  with a trend which changes from linear to nonlinear because of the influence of TPA. This dependence

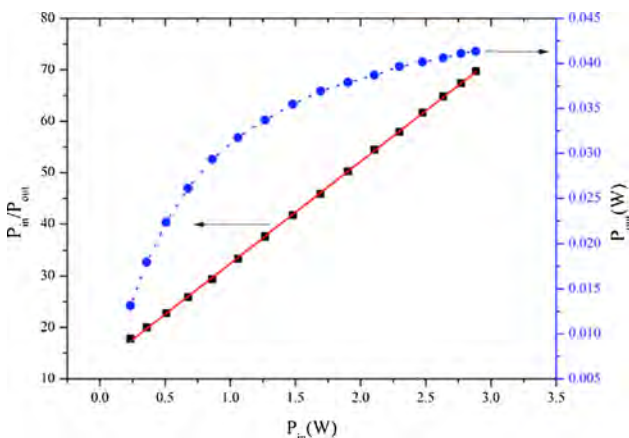
can be expressed by

$$P_{in}/P_{out} = (e^{\alpha_0 L} L_{eff} \beta / A_{eff}) P_{in} + e^{\alpha_0 L}, \quad (4)$$

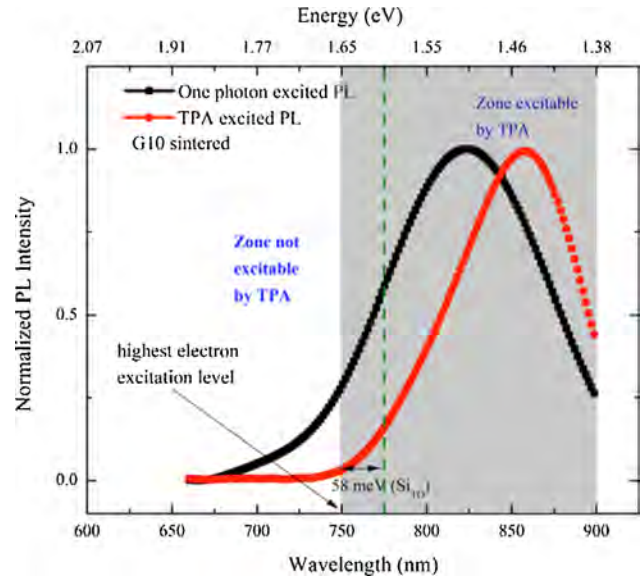
where  $L_{eff} = (1 - e^{-\alpha_0 L})/\alpha_0$ ,  $L$  is the waveguide length and  $A_{eff}$  is the effective mode area of the waveguide.  $A_{eff}$  can be computed by finite-element methods employing COMSOL multiphysics. In particular, the fit of  $P_{in}/P_{out}$  as a function of  $P_{in}$  yields  $\beta$  and  $\alpha_0$ .

Figure 5 shows  $P_{out}$  versus  $P_{in}$  as well as  $P_{in}/P_{out}$  versus  $P_{in}$  with the linear fit for a Si-nc waveguide (sample parameters in [25]). Calculated values of  $\beta$  at 1550 nm are of the order  $10^{-8}$ – $10^{-9}$  cm  $W^{-1}$ , which is more than one order of magnitude larger than the bulk-silicon value [26]. We have noticed changes in  $\beta$  as the Si content varies. This indicates that quantum confinement effects are also relevant for TPA. When the Si-nc waveguides are pumped by a 1550 nm picosecond laser, TPA excites carriers in the Si-nc. These relax quickly to the minima of the excited-state band and decay to the ground state either by photon emissions or by nonradiative processes. Therefore, it is possible to excite PL by subbandgap excitation provided that TPA is strong. In fact, we measured PL emission due to TPA from the surface of the waveguides (Fig. 6).

It is also possible to use the TPA-induced PL to map the spatial multimode interference profile of a multimode Si-nc waveguide. The concept is that the observation of the TPA-excited PL emitted from the waveguide is a monitor of the intensity of the field of the propagating optical mode. Figure 7a–d shows the multimode maps for a 10  $\mu$ m wide Si-nc waveguide. A decrease is observed of the TPA-induced PL emission with the distance due to the signal depletion caused by the nonlinear absorption. The clear oscillations in the TPA-assisted PL signal are due to the interference of the propagating 1550 nm optical modes in our multimode waveguide. These are also observed in the spatial map of the TPA-induced PL (Fig. 7c and d).



**Figure 5** (a)  $P_{out}$  and  $P_{in}/P_{out}$  versus  $P_{in}$  for a 1.5  $\mu$ m wide Si-nc waveguide. The red continuous line is a fit of the data with Eq. (4). From Ref. [25].



**Figure 6** One- and two-photon-induced PL from a Si-nc waveguide. The vertical dashed line is twice the energy of 1550 nm photons. Note that the onset of the TPA-excited PL is about one TO phonon energy higher than twice the energy of 1550 nm photons. From Ref. [25].

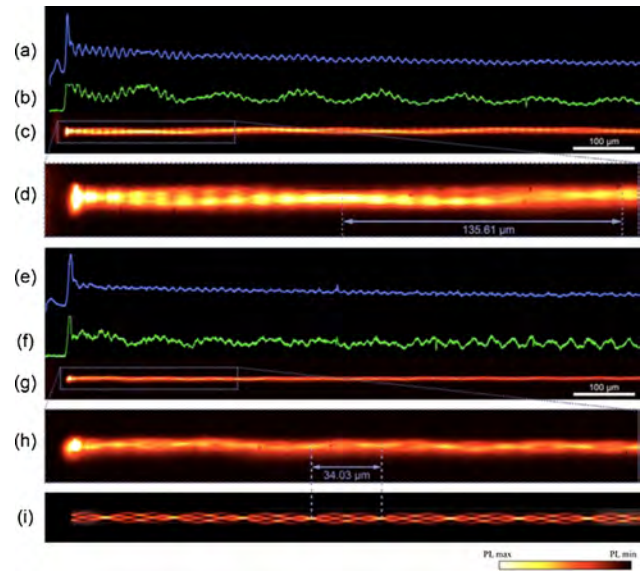


**Figure 7** (a) Integrated intensity profile of the TPA-induced PL along the length of the waveguide. Data refer to a 10  $\mu$ m wide Si-nc waveguide. (b) Intensity profile of the TPA-excited PL along waveguide length corresponding to a line scan through the center of the waveguide. (c) TPA-induced PL image of the waveguide. (d) Same as (c) but with an increased magnification. The arrow refers to the beat length. (e) Integrated intensity profile of the TPA-excited PL along the length of the waveguide. Data refer to a 5  $\mu$ m wide Si-nc waveguide. (f) Intensity profile of the TPA-excited PL along the waveguide length corresponding to a line scan through the center of the waveguide. (g) TPA-induced PL image of the waveguide. (h) Same as (g) but with an increased magnification. The arrow refers to the beat length. (i) COMSOL multiphysics FEM simulation for the 5  $\mu$ m waveguide. From Ref. [25].

Figure 7e–h report the same information for a 5  $\mu\text{m}$  wide multimode Si-nc waveguide. A comparison with the multimode interference (MMI) pattern simulated using FEM for this specific waveguide is shown in Fig. 7i. The agreement between the measured mode profile and the simulated one is remarkable. For the 5 and 10  $\mu\text{m}$  waveguides, the beat lengths of the MMI pattern have been found to be 34 and 135.6  $\mu\text{m}$ , respectively, which agree with the theoretical beat lengths. In this way, the simple observation of the luminescence (induced by two-photon absorption) allows mapping of the intensity profiles of the propagating optical modes inside the multimode waveguide with a higher resolution than that obtained by using the scattered light at 1550 nm.

**3.2 Optical bistability** The nonlinear refractive index, i.e., the light-intensity dependence of the refractive index, is caused by various effects: the thermo-optic effect (TOE), the excited-carrier dispersion (ECD, mediated by TPA), and the third-order nonlinear Kerr effect [27]. These three processes are characterized by different time scales. The Kerr effect is very fast, while TOE and ECD are slower. A light intensity dependent refractive index,  $n(I) = n_0 + n_2I$ , in a microdisk resonator leads to an intensity-dependent resonance position of the WGM modes. One of the manifestations of this is the optical bistability (OB) that is observed when performing nonlinear optical experiments with microdisks. To study the thermo-optically induced bistability (thermo-OB) in a fully integrated Si-ncs microdisk resonator, we have used a vertical coupling scheme between the Si-ncs microdisk resonator and a buried SiON bus waveguide. The thermo-OB is observed by using the CW pump power-dependent transmission at a specific pump wavelength ( $\lambda_p$ ) red-detuned from the cold cavity resonance ( $\lambda_m$ ), i.e.,  $\lambda_p > \lambda_m$ . Specifically, Fig. 8 shows the bus waveguide transmission when the pump power is swept from 115  $\mu\text{W}$  to 97 mW. An increase in the input power increases  $n_{\text{eff}}$  of the resonance mode. This induces a shift of

the resonance position towards the laser wavelength. As a consequence, the cavity internal field becomes stronger, which in turn decreases further the separation between  $\lambda_p$  and  $\lambda_m$ . At a certain power threshold  $P_{\text{th1}}$ , a positive feedback is initiated and the cavity mode is locked to the pump position, resulting in a sharp fall in the transmitted signal. This locking persists with a further increase in the pump power. On decreasing the input power, the cavity internal field is intense enough to maintain the resonance spectral position near to the pump one, until a second threshold power  $P_{\text{th2}}$ , lower than  $P_{\text{th1}}$ , occurs where the resonator cools down. At this point, the resonance unlocks and the transmission jumps to the high transmission state.

Therefore, a hysteresis loop is formed (Fig. 8). The device has two different stable states for the same input power, the system is bistable. The estimated thermo-optical coefficient  $dn/dT$  of the Si nanocrystalline material, using the substrate temperature-dependent resonator peak position, is estimated to be  $2.92 \times 10^{-5} \text{ K}^{-1}$ , which is an order of magnitude lower than that of bulk silicon and similar to that of fused silica. Also, modulated pump measurements were performed to determine the temporal response of the heat dissipation from the cavity. Figure 9a shows the time evolution of the modulated input pump beam (500 kHz, 50% duty cycle at 1551.8 nm) (blue curve), the transmitted pump (red), and the probe (black) signals (1533.8 nm). The measured probe fall time is  $645 \pm 9 \text{ ns}$ . These values are similar to those reported on smaller microrings patterned on SOI substrates [29, 30] and about three orders of magnitude smaller than those reported on free-standing silicon microresonators [31]. This time-resolved pump–probe experiment along with the temperature mapping of the resonator using numerical finite-element simulations (Fig. 9b) confirm that the silica host is responsible for the heat dissipation from the resonator.

**3.3 All-optical switching** An all-optical switch is a device where one optical signal is controlled by another optical signal, i.e., light is controlled by light [27]. In this case, we are interested in a fast response, so that we consider the Kerr nonlinearity of Si-nc. The idea is to tune the microring resonator in and out of resonance by a refractive-index change caused by the Kerr effect. A high-intensity pump beam is the responsible of the resonance shift, whereas a relatively weaker probe beam is used to monitor the ON–OFF states. The microring is based on a horizontal slot waveguide composed by two Si waveguides (245 nm in height) separated by a thin layer (45 nm) of Si-nc/SiO<sub>2</sub> (Fig. 10).

In such a waveguide topology, the field is concentrated in the intermediate area that corresponds to the Kerr medium. As a result, the nonlinearities are drastically enhanced by field confinement. The pump signal was modulated at 10 GHz using a 40 Gbit/s pattern generator through an electro-optic modulator. At the modulator output, the pulse width was estimated to be about 10 ps. In the experiment, the CW probe signal detuning from the

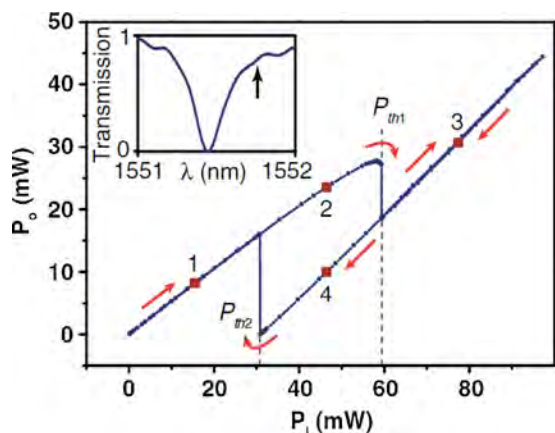


**Figure 8** Transmitted power versus input power. The arrows indicate the sweeping direction. Inset: cold resonance transmission spectrum. The arrow points to the pump laser position. From Ref. [28].

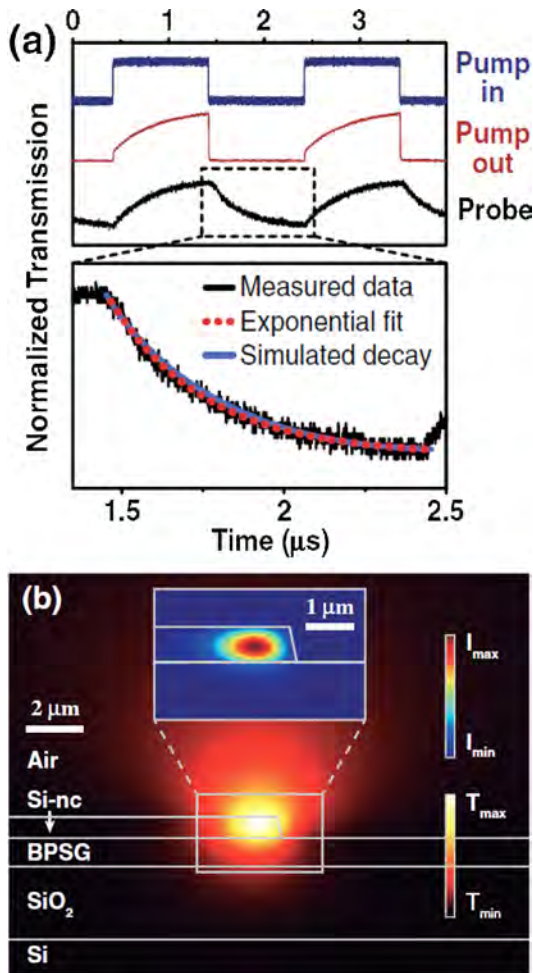


**Figure 9** (a) Top panel: the modulated pump transmission measurements of the input pump beam, the output pump signal, and the probe signal. Bottom panel: a magnification of the probe signal decay, the fit curve, and the FEM model result. (b) The calculated temperature map profile of the resonator. The inset shows the optical energy-density distribution employed in the FEM simulations for the heat dissipation. From Ref. [28].

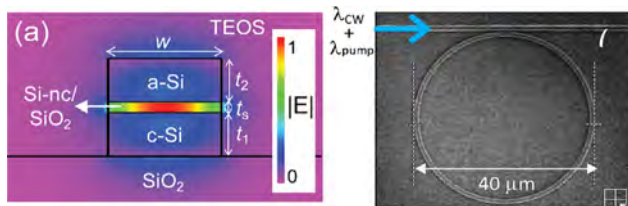


**Figure 10** (a) Schematic cross section of the slot waveguide. The slot is filled with Si-nc/SiO<sub>2</sub> sandwiched between upper amorphous a-Si and lower crystalline c-Si layers. The whole waveguide is placed over a SiO<sub>2</sub> layer and covered by tetra-ethyl-ortho-silicate (TEOS). The computed electric-field distribution for quasi-TM polarization corresponding to  $t_1 = t_2 = 220$  nm,  $t_s = 50$  nm,  $w = 500$  nm, and a 0.08 silicon excess is shown. (b) Scheme of the switching structure showing an SEM image of the microring of 40 μm diameter coupled with the bus waveguide. From Ref. [32].

cavity resonance (red-detuning or blue-detuning) depends on the average pump power because of the system thermalization. As a result, ultrafast peaks or dips, in the probe time-response, due to a Kerr red-shift are observed on arrival of the pump pulses. Consequently, the probe output also becomes pulsed following the pump one (Fig. 11a). In this case, the measured probe pulse width is about 11 ps and the extinction ratio is 2.2 dB (40% modulation depth). Increasing the pump peak power to bring the resonance peak exactly at the probe wavelength makes a transmission modulation of 3.6 dB (more than 50%). Thus, the ultrafast nonlinear response of the all-optical switching structure is demonstrated.

Actually, this ultrafast Kerr phenomenon has been observed superimposed on a slow (few nanoseconds) and weak (1 dB) modulation originated by the parasitic dispersion due to the excited carriers present inside the microring (Fig. 11a). As a conclusion, the above results show the feasibility of ultrafast all-optical switching devices employing Si-nc.

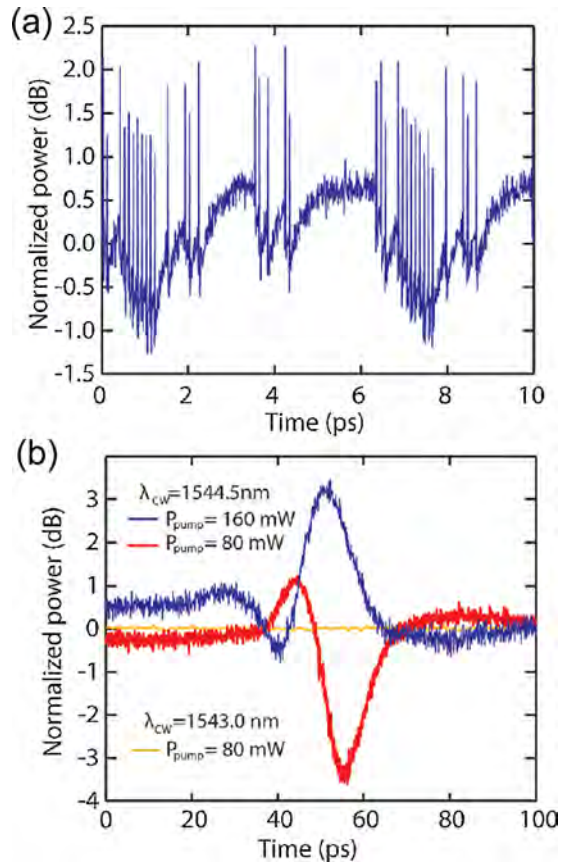


**Figure 11** Temporal response of the transmitted probe signal corresponding to an input pump pulsed at 40 Gbit/s. In (a), the on-chip pump peak power ( $P_{pump}$ ) is 150 mW and  $\lambda_{pump} = 1557.5$  nm. In (b) each curve corresponds to different values of  $P_{pump}$  and  $\lambda_{CW}$  (indicated in the figure). The normalized peak or dip response of the system depends on the relative probe position with respect to the different thermalized response of the resonance. From Ref. [32].

**3.4 Four-wave mixing** Four-wave mixing (FWM) is a third-order nonlinear parametric process [27]. As the name implies, four waves are combined through the nonlinear material. The phenomenon is usually manifested in its degenerate form, where two photons of a high-power signal (pump) are combined with one single photon of a reference signal (signal) into a nonlinear material generating a new photon of the third signal (idler). In this parametric process, the energy conservation is strictly maintained. Thus, the frequency of the idler is determined by the frequency difference between pump and signal frequencies ( $\omega_i = 2\omega_p - \omega_s$ , being  $\omega_p, \omega_s$  and  $\omega_i$  the frequency of the pump, signal, and idler, respectively). There is already remarkable progress for efficient frequency conversion in optical fibers, silicon waveguides, silicon nitride waveguides as well as Si-nc slot waveguides. Here, we investigate FWM in a Si-nc channel waveguide at 1550 nm.

For an efficient FWM, one has to match the frequencies as well as the phases of the propagating waves. The net phase mismatch term is  $\kappa = 2\gamma P_p - \Delta\beta$ , where  $\gamma = n_2\omega_p/cA_{\text{eff}}$  and  $\Delta\beta = 2\beta_p - \beta_s - \beta_i$  is the linear phase mismatch term. In order to get  $\kappa = 0$ , an anomalous group velocity dispersion ( $\beta_2 < 0$ ) is tailored by engineering the waveguide geometry (Fig. 12). Dispersion curves for the fundamental TE mode are shown in Fig. 13 for Si-nc waveguides having a fixed height of 800 nm and various widths.

The efficiency of FWM is measured by the idler conversion efficiency  $\eta = P_i(L)/P_s(0)$ , where  $P_i(L)$  and  $P_s(0)$  are the powers of the idler at the exit ( $L$ ) and of the signal mode at the input of the waveguide. In this context, it is useful to define a normalized conversion efficiency ( $\eta_{\text{norm}}$ ) to make it independent of the input pump power ( $P_{\text{pump}}$ ) and waveguide length:  $\eta_{\text{norm}} = 100 \times (P_{\text{idler}}/P_{\text{signal}})/P_{\text{pump}}$ . For the waveguide under study, a variation of the signal wavelength for a fixed pump wavelength close to 1550 nm gives rise to symmetric idler generation (Fig. 14). This is associated with a conversion

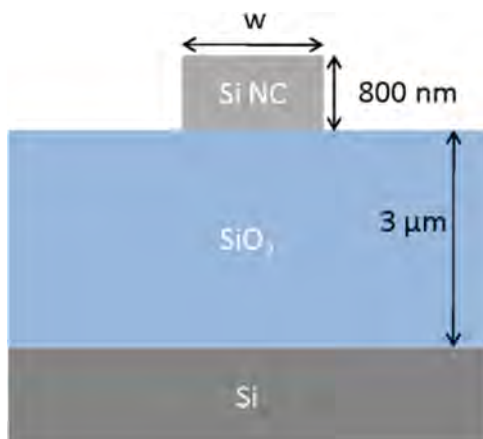


**Figure 12** Typical structure of our Si-nc channel waveguide employed for the degenerate FWM experiment.  $w = 1.08 \mu\text{m}$ .

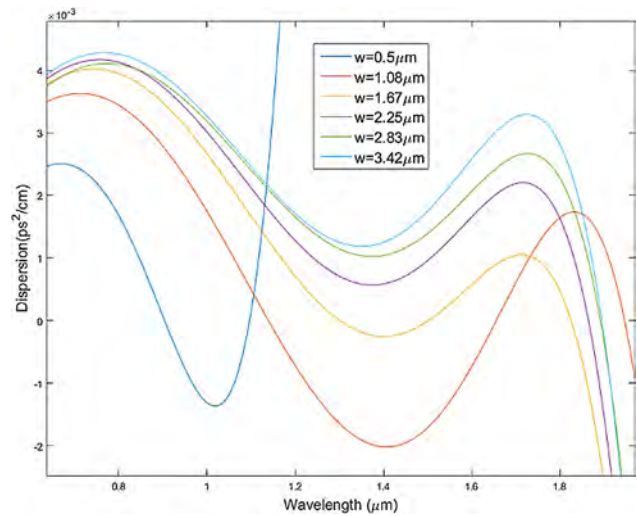


**Figure 13** Group-velocity dispersion ( $\beta_2$ ) for Si-nc channel waveguide with variable widths keeping fixed height of 800 nm for the fundamental TE mode.

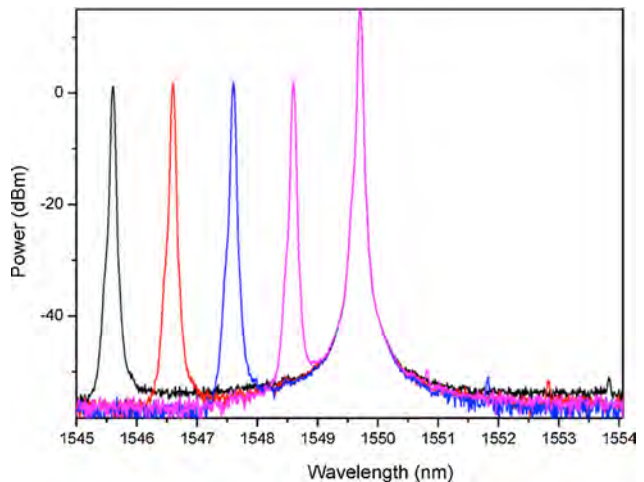


**Figure 14** Optical spectra acquired by an optical spectrum analyzer. Pump is fixed close to 1550 nm, and the signal is varied in between 1545 and 1550 nm, so that the idler frequencies are generated on the opposite side of the pump. Signal to idler conversion efficiency comes out to be  $-50 \text{ dB}$ .

efficiency of  $-50 \text{ dB}$  at a pump input power of 24 mW. When the length of the waveguide is 4 mm, the normalized efficiency is 0.15%. The large effective area of such waveguides could be the explanation for these low efficiencies. However, it is optimistically expected that by using longer waveguides, the conversion efficiency can be enhanced by several times.

**4 Silicon nanocrystal-based LED** Si-nc are formed in a dielectric, i.e., in an insulating matrix. Therefore, current injection can only occur via tunneling processes. To improve injection, different geometries of the gate oxide of

metal oxide semiconductor (MOS) light-emitting devices (LED) have been realized. To enhance the LED power efficiency alternating stoichiometric SiO<sub>2</sub> and SRO layers containing large Si excess have been used [33].

In many devices, light emission under DC condition and at high voltages is due to impact excitation that follows a Fowler–Nordheim (FN) tunneling injection. FN tunneling is the tunneling through the triangular barrier that the SiO<sub>2</sub> conduction band forms under a high bias. Therefore, the carriers are directly excited into the oxide and, as hot carriers, impact the Si-nc where they cool down by giving back the excess energy to generate an electron–hole pair. The prolonged action of this mechanism damages the device leading to the failure of the device. The spectral emission of Si-nc-based LEDs has been explained as due to a multicenter origin of the electroluminescence (EL) linked to interface states as well as exciton recombination in Si-nc [34]. Moreover, sequential FN injection of electrons and holes into Si-nc by means of an alternating pumping scheme has been used to reach higher LED power efficiencies [35].

To get direct tunneling, we proposed to use a multilayer structure where alternate nanometer-thick layers of SiO<sub>2</sub> and Si-nc yield controlled tunneling barriers [36]. In this way, we demonstrated bipolar injection via direct tunneling at low voltages under DC conditions. As an example, in the following, we consider two types of gate structures for the Si-nc LED: single layer and multilayer (Fig. 15).

The multilayer structure has some advantages over the single layer, such as a higher Si-nc density, more uniformity in the size of the Si-nc, lower turn-on voltages, higher current density at low-applied electric fields, higher EL intensity at the same injected current and higher power efficiency at low-applied currents [37]. While Si-nc grow randomly in a single layer, in a multilayer structure they are confined to grow between the two SiO<sub>2</sub> layers of the layer stack. This constrains their size to the SRO layer thickness. Therefore, the Si-nc size distribution is strongly reduced in a multilayer sample with respect to a thick single layer one.

To further improve the power efficiency, we used the concept of injection rate engineering by grading the size of the Si-nc in the multilayer (Fig. 16). The resulting structure is a graded-gap multilayer with a step-by-step decrease in the SRO thickness toward the center of the multilayer (Fig. 16a). As can be seen in Fig. 16b, the energy bands of

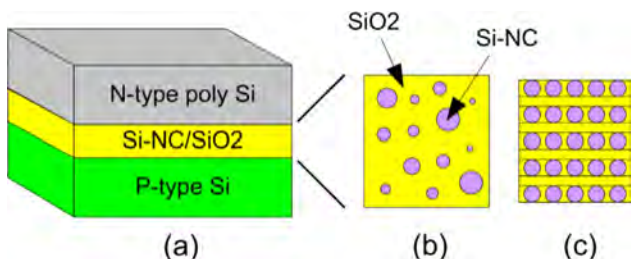


**Figure 15** (a) The MOS structure of Si-nc LED, (b) the single-layer active area, and (c) the multilayer active area.

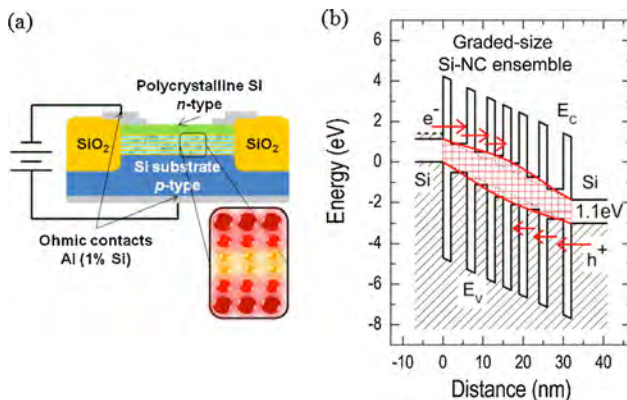


**Figure 16** (a) Scheme of the graded-gap multilayer Si-nc LED structure and (b) the energy-band diagram for the Si-nc ensemble [11].

the graded-gap multilayer align at low forward bias voltages. This alignment facilitates the tunneling of charges into the central recombination region that contains small Si-ncs. In turn, small Si-nc have a high-radiative recombination efficiency, which explains the high-power efficiency of graded-gap LED.

The EL of the graded-gap Si-nc LED is higher than that of devices with single layer and multilayer active areas (Fig. 17a). In addition, there is an improvement in charge injection in the graded-gap Si-nc LED compared to the multilayer device (Fig. 17b): at the same applied voltage, the current density in the graded-gap Si-nc LEDs is higher than that of the multilayer device. This proves that the bandgap engineering results in an easy carrier injection into the small nanocrystals in the central part of the active area. The graded-gap structure possesses both the qualities of high-electrical conductivity and high-luminescence attributed to large Si-ncs and small Si-ncs, respectively [38].

By investigating the devices under AC condition, we found that the injection dynamics of electrons and holes in Si-ncs is strongly dependent on the bias waveforms. Under forward bias, electrons and holes tunnel within the gate dielectric and can be separately trapped in Si-nc or reach concurrently the same Si-nc where they recombine. When the bias is abruptly switched off or turned abruptly to reverse bias, the trapped charges diffuse toward large Si-ncs, generating an EL overshoot that decays with the characteristics times of unbiased Si-nc (Fig. 18).

### 5 Quantum random number generator based on silicon nanocrystals

The importance of secure communication and cryptography has been realized for a long time and is acknowledged even more profoundly in today’s modern world. Producing confidential messages that are totally protected from the access of third parties is a requisite to guarantee safe data transmission. Random numbers play a key role in this area and, hence, generation of completely unpredictable, truly random numbers is needed.

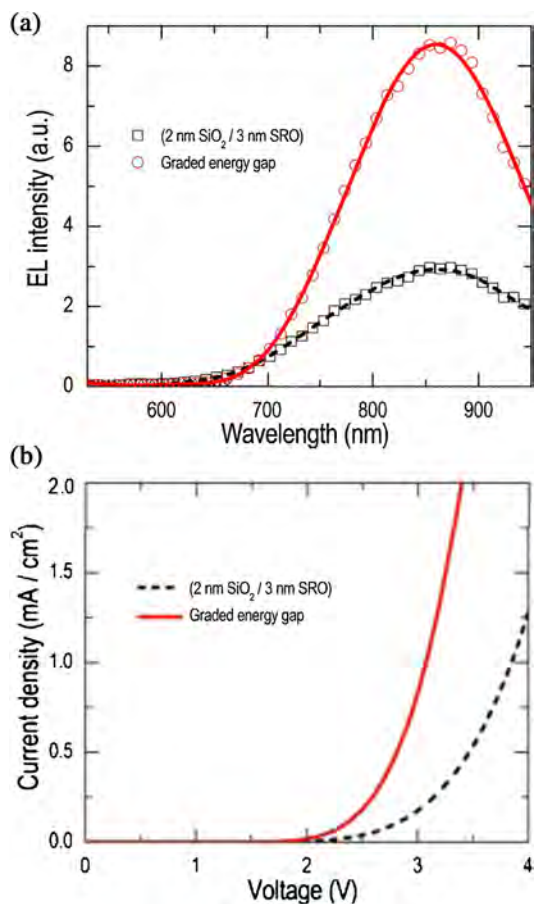


**Figure 17** (a) EL spectra and (b) forward  $I$ - $V$  characteristics of multilayer Si-nc LEDs with 2 nm SiO<sub>2</sub>/3 nm and the graded-gap LED with decreasing SRO thickness of 4–3–2 nm.

Truly random numbers are necessarily produced through physical nondeterministic processes, as the unpredictability of commonly used random-like numbers generated by mathematical, deterministic algorithms is refutable. Quantum physics happens to be greatly beneficial in this area due to the existence of intrinsic randomness in quantum phenomena.

Different approaches have been considered benefiting from the quantum effects in the sources of entropy [39–41]. One example is light emission in a LED. LEDs are based on the spontaneous emission of photons, which is a statistically random process. Therefore, the Si-nc LED can be considered a quantum source of entropy. This approach is the one we will describe in the following. We used a simple setup based on a Si-nc LED, a Si single-photon avalanche photodiode (SPAD) and a multichannel scaler (MCS) to acquire sequences of data (Fig. 19). A description of the setup and data acquisition can be found in our recent study [42].

To evaluate the randomness of the generated data sequences, we used the NIST test suite [43]. Running these tests enables detection of deviations of a binary sequence from randomness. A random bit sequence resembles the outcome of the flips of an unbiased, fair coin with

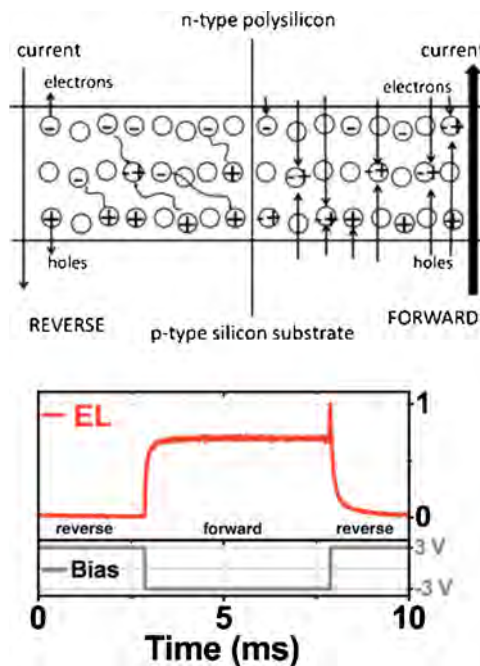


**Figure 18** (Top) Schematic of the injection phenomena used to explain the experimental outcomes. (Bottom) Time-resolved EL measurement carried out on the studied samples. At the bottom of the plot the bias scheme used to drive the device is illustrated.

sides labeled “0” and “1,” with a probability of exactly 1/2 of producing a “0” or “1.” The flips are independent of each other, meaning that the result of any previous coin flip does not affect future coin flips. Therefore, in a perfect random sequence all the elements are generated independently of each other and the knowledge of a value in a sequence does not result in the prediction of the following values.

Using the setup schematically illustrated in Fig. 19 for data acquisition, we demonstrated that the obtained data has a Poisson distribution and then made use of the survival function to adjust the parameters in the experiment

$$\lambda t_w = \ln(2), \quad (5)$$

where  $t_w$  is the observation window (bin width) and  $\lambda$  the average number of observed photons per unit time.

Having fixed the bin width, we calculated the average number of photons using Eq. (5). In order to achieve the proper photon flux we fixed the voltage (current) of the LED. Figure 20 shows the EL of a Si-nc LED as a function of

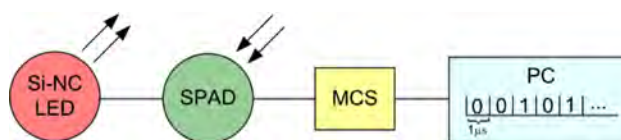


**Figure 19** Scheme of the setup used to obtain sequences of data. Here the emission from a Si-nc LED is detected by a silicon single-photon avalanche photodiode (SPAD) and recorded by a multichannel scaler (MCS) to generate a random bit sequence.

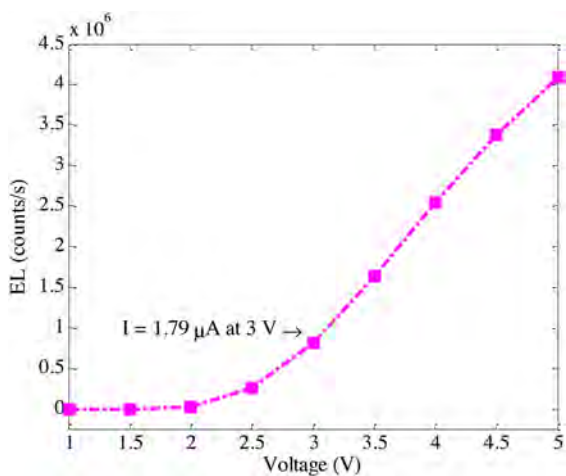


**Figure 20** Electroluminescence versus voltage for a Si-ncs LED.

voltage. To cause minimum degradation to the oxide layers in the active area of Si-nc LED, the applied voltage should be kept below about 3 V, which implies that the applied current needs to be kept below 1.79  $\mu\text{A}$ .

The photon arrivals from the Si-nc LED were detected using the MCS and the number “1” was attributed to the detection of at least one photon in the fixed time window and “0” to the detection of no photon. One main advantage of the proposed approach is the negligible bias ( $\sim 0.0013$ ) measured from the short datasets of  $10^8$  bits length. This allows the production of sequences to pass the NIST frequency test without any deterministic postprocessing algorithms. The frequency test is the first and most important test in the NIST test suite that determines whether the number of ones and zeros are approximately the same, as would be expected from a random sequence.

However, the only test in NIST test suite that fails with our setup is the Runs test. By reinforcing an artificial dead time equal to the bin width and half the bin width, we were able to remove the correlation between consecutive bits and consequently our sequences passed the Runs test as well as the others without having to apply any postprocessing operations. The maximum bit rate of the QRNG is 0.6 Mbps. Higher bitrates can be achieved by the parallelization of the LEDs and detectors.

**6 Conclusions** The use of silicon nanocrystals in photonics has been reviewed here with two main examples in nonlinear optics and in quantum random number generations. Quantum size effects change the properties of Si-nc with respect to bulk silicon, which allows enlarging the phenomenology and the application spectrum of silicon photonics.

**Acknowledgements** This work was supported by the Provincia Autonoma di Trento through the “bando grandi progetti 2014 SIQURO.” M. G and G. P. acknowledge the support of the Microfabrication Laboratory staff of FBK during sample fabrication.

## References

- [1] L. Vivien and L. Pavesi (eds.), Handbook of Silicon Photonics, (CRC Press, Taylor and Francis Group, New York, 2013).
- [2] <https://communities.intel.com/community/itpeernetwork/datastack/blog/2014/03/10/mxc-technology-will-light-up-21st-century-data-centers>.
- [3] <http://www.ict-iris.eu/index.html>.
- [4] [http://researcher.watson.ibm.com/researcher/view\\_group.php?id=2757](http://researcher.watson.ibm.com/researcher/view_group.php?id=2757).
- [5] L. Pavesi and R. Turan (eds.), Silicon Nanocrystals; Fundamentals, Synthesis and Applications (Wiley-VCH Verlag GmbH, Berlin, 2010).
- [6] E. J. Henderson, J. A. Kelly, and J. C. G. Veinot, Chem. Mater. **21**, 5426 (2009).
- [7] M. L. Mastronardi, F. Maier-Flaig, D. Faulkner, E. J. Henderson, C. Kubel, U. Lemmer, and G. A. Ozin, Nano Lett. **12**, 337 (2011).
- [8] F. Maier-Flaig, J. Rinck, M. Stephan, T. Bocksrocker, M. Bruns, C. Kübel, A. K. Powell, G. A. Ozin, and U. Lemmer, Nano Lett. **13**, 475 (2013).
- [9] L. Pavesi, L. Dal Negro, C. Mazzoleni, G. Franzo, and F. Priolo, Nature **408**, 440 (2000).
- [10] R. Spano, N. Daldosso, M. Cazzanelli, L. Ferraioli, L. Tartara, J. Yu, V. Degiorgio, E. Giordana, J. M. Fedeli, and L. Pavesi, Opt. Express **17**, 3941–3950 (2009).
- [11] Z. Yuan, A. Anopchenko, and L. Pavesi, in: Advanced Silicon Materials for Photovoltaic Applications, edited by S. Pizzini (John Wiley and Sons Ltd., 2012), chap. 10, pp. 355–391.
- [12] F. Sgrignuoli, P. Ingenhoven, G. Pucker, V. D. Mihailtchi, E. Froner, Y. Jestin, E. Moser, G. Sánchez, and L. Pavesi, Sol. Energy Mater. Sol. Cells **132**, 267–274 (2015).
- [13] S. Chinnathambi, S. Chen, S. Ganesan, and N. Hanagata, Adv. Healthcare Mater. **3**, 10 (2014).
- [14] N. Daldosso, A. Ghafarinazari, P. Cortelletti, L. Marongiu, M. Donini, V. Paterlini, P. Bettotti, R. Guider, E. Froner, S. Dusi, and M. Scarpa, J. Mater. Chem. B **2**, 6345 (2014).
- [15] A. J. Kenyon, Prog. Quantum Electron. **26**, 225 (2002).
- [16] R.-J. Zhang, S.-Y. Seo, A. P. Milenin, M. Zacharias, and U. Gösele, Appl. Phys. Lett. **88**, 153120 (2006).
- [17] R. D. Kekatpure and M. L. Brongersma, Phys. Rev. A **78**, 023829 (2008).
- [18] M. Ghulinyan, D. Navarro-Urrios, A. Pitanti, A. Lui, G. Pucker, and L. Pavesi, Opt. Express **16**, 13218 (2008).
- [19] M. Ghulinyan, A. Pitanti, G. Pucker, and L. Pavesi, Opt. Express **17**, 9434 (2009).
- [20] D. Navarro-Urrios, A. Pitanti, N. Daldosso, F. Gourbilleau, R. Rizk, G. Pucker, and L. Pavesi, Appl. Phys. Lett. **92**, 051101 (2008).
- [21] R. G. Elliman, M. Forcales, A. R. Wilkinson, and N. J. Smith, Nucl. Instrum. Methods Phys. Res. B **257**, 11 (2007).
- [22] A. Pitanti, M. Ghulinyan, D. Navarro-Urrios, G. Pucker, and L. Pavesi, Phys. Rev. Lett. **104**, 103901 (2010).
- [23] E. M. Purcell, Phys. Rev. **69**, 681 (1946).
- [24] J. M. Gérard, B. Sermage, B. Gayral, B. Legrand, E. Costard, and V. Thierry-Mieg, Phys. Rev. Lett. **81**, 1110 (1998).
- [25] S. Manna, F. Ramiro-Manzano, M. Ghulinyan, M. Mancinelli, F. Turri, G. Pucker, and L. Pavesi, Appl. Phys. Lett. **106**, 071109 (2015).
- [26] X. Sang, E.-K. Tien, and O. Boyraz, J. Optoelectron. Adv. Mater. **11**, 15 (2008).

- [27] R. W. Boyd, *Nonlinear Optics* (Academic Press, Boston, 1992).
- [28] F. Ramiro-Manzano, N. Prtljaga, L. Pavesi, G. Pucker, and M. Ghulinyan, *Opt. Lett.* **38**, 3562 (2013).
- [29] Q. Xu and M. Lipson, *Opt. Lett.* **31**, 341 (2006).
- [30] V. R. Almeida and M. Lipson, *Opt. Lett.* **29**, 2387 (2004).
- [31] P. Sun and R. M. Reano, *Opt. Lett.* **35**, 1124 (2010).
- [32] A. Martínez, J. Blasco, P. Sanchis, R. Spano, J. V. Galán, J. García, J. M. Martínez, E. Jordana, P. Gautier, Y. Lebour, R. Guider, P. Pellegrino, S. Hernández, N. Daldosso, B. Garrido, J. M. Fedeli, L. Pavesi, and J. Martí, *Nano Lett.* **10**, 1506 (2010).
- [33] A. Anopchenko, A. A. Prokofiev, I. N. Yassievich, S. Ossicini, L. Tsybeskov, D. J. Lockwood, S. Saeed, T. Gregorkiewicz, M. Wojdak, J. Liu, and A. Meldrum, *Silicon-Based Light Sources*, see [1], chap. 3.
- [34] S. Godefroo, M. Hayne, M. Jivanescu, A. Stesmans, M. Zacharias, O. Lebedev, G. Van Tendeloo, and V. V. Moshchalkov, *Nature Nanotechnol.* **3**, 174–178 (2008).
- [35] R. J. Walters, G. I. Bourianoff, and H. A. Atwater, *Nature Mater.* **4**, 143–146 (2005).
- [36] A. Marconi, A. Anopchenko, M. Wang, G. Pucker, P. Bellutti, and L. Pavesi, *Appl. Phys. Lett.* **94**, 221110 (2009).
- [37] M. Wang, A. Anopchenko, A. Marconi, E. Moser, S. Prezioso, L. Pavesi, G. Pucker, P. Bellutti, and L. Vanzetti, *Physica E* **41**, 912–915 (2009).
- [38] A. Anopchenko, A. Marconi, M. Wang, G. Pucker, P. Bellutti, and L. Pavesi, *Appl. Phys. Lett.* **99**, 181108 (2011).
- [39] B. Qi, Y.-M. Chi, H.-K. Lo, and L. Qian, *Opt. Lett.* **35**, 312–314 (2010).
- [40] C. Gabriel, C. Wittmann, D. Sych, R. Dong, W. Mauerer, U. L. Andersen, C. Marquardt, and G. Leuchs, *Nature Photon.* **4**, 711–715 (2010).
- [41] B. Sanguinetti, A. Martin, H. Zbinden, and N. Gisin, *Phys. Rev. X* **4**, 031056 (2014).
- [42] Z. Bisadi, A. Meneghetti, G. Fontana, G. Pucker, P. Bettotti, and L. Pavesi, in: *Proc. SPIE* **9520**, 952004 (2015).
- [43] <http://csrc.nist.gov/groups/ST/toolkit/rng/documents/SP800-22rev1a.pdf>.
- [44] F. Sanghaleh, I. Sychugov, Z. Yang, J. G. C. Veinot, and J. Linnros, *ACS Nano* **9**, 7097 (2015).